clean technologies

MDPI

Article

Iron and Magnesium Impregnation of Avocado Seed Biochar for Aqueous Phosphate Removal

Jihoon Kang [1,*], Jason Parsons [2], Sampath Gunukula [3] and Dat T. Tran [4]

[1] School of Earth, Environmental and Marine Sciences, University of Texas Rio Grande Valley, Edinburg, TX 78539, USA
[2] Department of Chemistry, University of Texas Rio Grande Valley, Brownsville, TX 78500, USA
[3] Forest Bioproducts Research Institute, University of Maine, Orono, ME 04469, USA
[4] DEVCOM Army Research Laboratory, Sensors and Electron Devices Directorate, Adelphi, MD 20783, USA
* Correspondence: jihoon.kang@utrgv.edu

Abstract: There has been increasing interest in using biochar for nutrient removal from water, and its application for anionic nutrient removal such as in phosphate (PO_4^{3-}) necessitates surface modifications of raw biochar. This study produced avocado seed biochar (AB), impregnated Fe- or Mg-(hydr)oxide onto biochar (post-pyrolysis), and tested their performance for aqueous phosphate removal. The Fe- or Mg-loaded biochar was prepared in either high (1:8 of biochar to metal salt in terms of mass ratio) or low (1:2) loading rates via the co-precipitation method. A total of 5 biochar materials (unmodified AB, AB + High Fe, AB + Low Fe, AB + High Mg, and AB + Low Mg) were characterized according to their selected physicochemical properties, and their phosphate adsorption performance was tested through pH effect and adsorption isotherm experiments. Fe-loaded AB contained Fe_3O_4, while Mg-loaded AB contained $Mg(OH)_2$. The metal (hydr)oxide inclusion was higher in Fe-loaded AB. Mg-loaded AB showed a unique free O–H functional group, while Fe-loaded AB showed an increase in its specific surface area more than 10-times compared to unmodified AB (1.8 m^2 g^{-1}). The effect of the initial pH on phosphate adsorption was not consistent between Fe-(anion adsorption envelope) vs. Mg-loaded AB. The phosphate adsorption capacity was higher with Fe-loaded AB in low concentration ranges ($\leq$50 mg L^{-1}), while Mg-loaded AB outperformed Fe-loaded AB in high concentration ranges (75–500 mg L^{-1}). The phosphate adsorption isotherm by Fe-loaded AB fit well with the Langmuir model (R^2 = 0.91–0.96), indicating the adsorptive surfaces were relatively homogeneous. Mg-loaded biochar, however, fit much better with Freundlich model (R^2 = 0.94–0.96), indicating the presence of heterogenous adsorptive surfaces. No substantial benefit of high loading rates in metal impregnation was found for phosphate adsorption. The enhanced phosphate removal by Mg-loaded biochar in high concentration ranges highlights the important role of the chemical precipitation of phosphate associated with dissolved Mg^{2+}.

Keywords: biochar; metal impregnation; phosphate adsorption; precipitation; pH effect

Citation: Kang, J.; Parsons, J.; Gunukula, S.; Tran, D.T. Iron and Magnesium Impregnation of Avocado Seed Biochar for Aqueous Phosphate Removal. *Clean Technol.* **2022**, *4*, 690–702. https://doi.org/10.3390/cleantechnol4030042

Academic Editor: Bin Gao

Received: 17 June 2022
Accepted: 19 July 2022
Published: 22 July 2022

1. Introduction

The nonpoint source pollution of nitrogen (N) and phosphorus (P) from agricultural and urban fields amended with fertilizer and manure has been recognized as a major contributor to human-induced eutrophication [1]. In particular, phosphate (PO_4^{3-}) is a limiting nutrient in aquatic ecosystems, and it is linked to accelerated eutrophication in surface waters [2]. The P-induced eutrophication causes excessive aquatic plant growth, blooms of harmful algae, and increased occurrence of anoxic conditions and fish deaths in surface waterbodies [3]. The US EPA recommends that the total P concentration not exceed 0.10 mg L^{-1} in streams not discharging directly into reservoirs and not exceed 0.05 mg L^{-1} in streams discharging directly into reservoirs [4].

Several treatment technologies are known to remove phosphate from water such as chemical precipitation using coagulants, anion exchange membranes, enhanced biological

uptake, and adsorption [5]. The most common method in water and wastewater treatment plants is chemical precipitation using ferric salts or alums, but its application generates a large volume of sludge and requires rigorous monitoring [5,6]. Adsorption has been proven to be a relatively simple, cost-effective method for removing phosphate [6–8]. Natural adsorbent (e.g., zeolite, limestone), industrial waste product (e.g., fly-ash, steel slag), and biochar have been used for phosphate removal [5,9]. Among them, biochar has been viewed as a promising adsorbent as it offers the possibility of adsorbent regeneration and slow-release fertilizer use [6–8]. Previous studies suggested that raw (unmodified) biochar without surface modifications was found to have limited or no adsorption capacity for oxyanions such as phosphate due to its net negative surface charge, causing electrostatic repulsion between the biochar's surface and phosphate ions [10–12].

Using the biochar as a base substrate to impregnate metal (hyr)oxides is a viable method to improve phosphate removal by altering surface properties such as hydroxylated functional groups [7,13]. The impregnation of biochar with metal oxides is achieved either before or after pyrolysis (pre-pyrolysis or post-pyrolysis) via chemical co-precipitation of the metal salts [13]. Raw biomass (pre-pyrolysis) or biochar (post-pyrolysis) is soaked into solutions of metal chloride to form metal oxide–biochar composites by raising the pH [13,14]. Frequently used metal salts include $FeCl_3$, $FeCl_2$, and $MgCl_2$ [13–19]. The advantage of Fe-loaded biochar is highlighted by its magnetic properties, which can facilitate its separation after use [6]. Magnesium (Mg) is considered as a suitable cation for metal impregnation due to its role in the chlorophyll formation of plants [20–22].

In this study, avocado seed was chosen as a biochar feedstock. With increasing global avocado production (6.4 million tons per year), avocado seed after processing (e.g., guacamole) is a substantial waste stream [23]. Note that local composting facilities do not accept avocado seeds because the hard seed can damage the mechanical grinder in the facility. Thus, making biochar using the avocado seed is an alternative way of recycling the seed waste. A recent study found that the avocado seed biochar (AB) was effective in removing aqueous lead [24].

The overall objective of this study was to examine the feasibility of Fe- or Mg-loaded AB as adsorbents for phosphate removal. This study employed the post-pyrolysis metal impregnation as it is applicable to existing raw biochar and the impregnation can be performed as needed. To the best of our knowledge, there was no study directly comparing the performance of Mg- vs. Fe-loaded biochar for phosphate removal via a post-pyrolysis approach. Specific objectives were to (1) examine the physicochemical properties of unmodified AB vs. Fe- or Mg-loaded AB under two contrasting loading levels, (2) determine the effect of the initial pH on phosphate adsorption, and (3) investigate phosphate adsorption behavior over varying concentration ranges (adsorption isotherm) affected by the metal impregnation.

2. Materials and Methods

2.1. Biochar Production

The Hass avocado (*Persea americana*) with dark-green-colored, bumpy skin was purchased from a local grocery store in South Texas, USA. Its typical weight was about 234 g, and its seed accounted for 15% of the weight (35 g). The collected seeds were rinsed with tap water, chopped in smaller sizes (1–2 cm), and oven-dried at 105 °C (Supplementary Figure S1). Dry avocado seed cuts were placed in a quartz crucible and were pyrolyzed at 400 °C in a muffle furnace for 2 h, which was found to be the optimal pyrolysis temperature for cationic heavy metal adsorption in previous studies [11,24]. The AB retained between the No. 10 sieve (2 mm) and No. 35 (0.5 mm) were collected, rinsed with deionized (DI) water, and oven-dried at 105 °C overnight for further use.

2.2. Metal-Loaded Biochar Preparation

Biochar–metal composites (metal-loaded AB) were produced under two metal loading levels by impregnating AB with Fe- or Mg-chlorides (Table 1). High and low metal loadings

(relative term) were based on the mass ratio of biochar to metal salt at 1:8 for high loading and 1:2 for low loading. These comparatively high metal loadings were chosen based on previous studies to ensure the metal impregnation of the AB [16,25–27]. For Fe-loaded AB preparation, Fe (III) chloride hexahydrate ($FeCl_3 \cdot 6H_2O$) and Fe (II) chloride tetrahydrate ($FeCl_2 \cdot 4H_2O$) were dissolved in DI water in 1:1 ratio, and AB was added to the Fe chloride solution similarly to the method of a previous study [28]. While being stirred for 30 min, an aqueous solution of 5 mol L^{-1} of NaOH was added to increase the pH (>10.0) in the suspension (Supplementary Figure S2). The suspension was rested overnight with no heating. The settled biochar–metal composites were collected through Whatman paper (Filter Paper 415), rinsed with DI water, and oven-dried at 105 °C for further use. Mg-loaded AB was prepared in a similar manner using Mg chloride hexahydrate ($MgCl_2 \cdot 6H_2O$) (Table 1; Supplementary Figure S3).

Table 1. Biochar and metal loadings for impregnation.

Metal Loaded AB	Constituents Added to 0.5 L of Deionized Water	Mass (g)	Metal Chloride (mmol L^{-1})
AB + High Fe	Raw avocado seed biochar (AB)	5	
	Fe (III) chloride hexahydrate ($FeCl_3 \cdot 6H_2O$)	20	148
	Fe (II) chloride tetrahydrate ($FeCl_2 \cdot 4H_2O$)	20	200
AB + Low Fe	Raw avocado seed biochar (AB)	5	
	Fe (III) chloride hexahydrate ($FeCl_2$ $6H_2O$)	5	37
	Fe (II) chloride tetrahydrate ($FeCl_2 \cdot 4H_2O$)	5	50
AB + High Mg	Raw avocado seed biochar (AB)	5	
	Magnesium chloride hexahydrate ($MgCl_2$ $6H_2O$)	10	394
AB + Low Mg	Raw avocado seed biochar (AB)	5	
	Magnesium chloride hexahydrate ($MgCl_2$ $6H_2O$)	40	98

2.3. Biochar Characterization

Unmodified and metal-loaded AB were characterized for their selected physicochemical properties. For the crystal structure of the biochar materials, X-ray diffraction (XRD) patterns were collected using a Bruker D2 X-ray diffractometer (Bruker, Billerica, Massachusetts, USA) from 10–80° in 2θ with a step of 0.05° and a 5 s counting time. The biochar's pH was measured by a pH meter (EC500, Extech Instruments, Waltham, MA, USA) in a 1:10 ratio of biochar-to-solution (DI water) after 1 h of equilibration [24]. The surface morphology of biochar samples was examined through a scanning electron microscope (SEM, ZEISS EVO LS10, Hitachi, Japan). The specific surface area of biochar samples was determined by the Brunauer–Emmett–Teller (BET) multilayer adsorption method via a surface area and porosity analyzer (Quantachrome Nova 2200e, Boynton Beach, FL, USA). Surface functional groups of the biochar materials were examined using a universal attenuated total reflectance Fourier transform infrared spectroscopy (UATR-FTIR) (Perkin-Elmer Frontier FTIR, Waltham, MA, USA). The FTIR spectra were obtained from the 4000 to 650 cm^{-1} region using an average of 32 scans at a resolution of 4 cm^{-1}. Proximate analysis was performed to determine volatile matter (mobile matter), fixed matter, and ash content in the biochar materials [28].

2.4. Initial pH Effect on Phosphate Adsorption

Biochar samples (0.1 g) were equilibrated with 30 mL of 10 mg L^{-1} phosphate solutions varying in initial pH (3, 5, 7, 9 and 11) for 24 h in duplicates. After the equilibration, the supernatants were filtered through 0.45 µm syringe filter and measured for their phosphate concentration by a HACH DR3900 spectrophotometer (HACH, Loveland, CO, USA) via

the HACH method 8114 (Molybdovanadate Method). The phosphate adsorption by the biochar samples (%) was calculated for data presentation.

$$\text{phosphate adsorption (\%)} = 100 \times (1 - C_f/C_0) \quad (1)$$

where C_0 is the initial concentration of phosphate in the solution (mg L^{-1}) and C_f is the final (equilibrium) concentration of phosphate in the solution after equilibration (mg L^{-1}).

2.5. Phosphate Adsorption Isotherm

For adsorption isotherm (room temperature ~20 °C and initial pH~6.5), 0.1 g of biochar was equilibrated with 30 mL of phosphate solutions at different concentrations (5, 10, 25, 50, 75, 100, 250 and 500 mg L^{-1}) for 24 h in duplicates. The supernatants were filtered through a 0.45 µm syringe filter and measured for their phosphate concentration using the aforementioned method. The amount of phosphate adsorbed by the biochar material (q in mg g^{-1}) was calculated by:

$$q = (C_0V - C_fV)/M \quad (2)$$

where C_0 is the concentration of phosphate in the initial solution (mg L^{-1}), V is the volume of liquid (L), and M is dry weight of biochar (g).

The adsorption data were fitted by two adsorption models (Langmuir and Freundlich). It is important to note that both adsorption isotherms models are based on macroscopic data, and they do not infer which retention mechanisms (e.g., adsorption or precipitation) are operating [29,30]. The Langmuir model is described by:

$$q = (S_{max}\ K_L C_f)/(1 + K_L C_f) \quad (3)$$

where S_{max} is the maximum adsorption capacity (mg g^{-1}) and K_L is an affinity constant to bonding energy (L g^{-1}). The Langmuir equation (Equation (3) can be rearranged for a linearized form:

$$C_f/q = 1/(K_L S_{max}) + C_f/S_{max} \quad (4)$$

A linear regression of C_f/q as a function of C_f yields the slope to be $1/S_{max}$ and the y-intercept as equal to $1/(K_L S_{max})$.

The Freundlich model is described by:

$$q = K_F\ (C_f)^{1/n} \quad (5)$$

where K_F is the Freundlich affinity coefficient ([mg g^{-1}]/[mg L^{-1}]$^{-1/n}$), n is the Freundlich linearity constant, and $1/n$ indicates the surface heterogeneity [27,31]. These parameters were determined using the linearized form of the Freundlich equation:

$$\log q = \log K_F + 1/n \log C_f \quad (6)$$

A linear regression between log q and log C_f yields the slope to be $1/n$ and the y-intercept to be log K_F.

For both isotherm models, Akaike Information Criterion (*AIC*) was estimated to examine the goodness of model fittings as a function of the sum of the squared errors [32,33]. Lower *AIC* values indicate a better-fitting model [33,34].

$$AIC = 2K + N\ \ln\left(\frac{SSE}{N}\right) + \frac{2K(K+1)}{N-K-1} \quad (7)$$

$$SSE = \sum_i^N \left(q_{experimental} - q_{model}\right)_i^2 \quad (8)$$

where K is the number of parameters of the adsorption model (K = 2), N is the number of experimental points (N = 8), SSE is the sum of squared errors, $q_{experimental}$ is the measured q value, and q_{model} is the fitted q value from the adsorption models.

3. Results and Discussion

3.1. Biochar Characterization

The XRD pattern for Fe-loaded AB (Figure 1) showed peaks corresponding to magnetite (Fe_3O_4), which showed the (111), (220), (311), (400), (422), (511), and (440) diffraction planes [35,36]. The magnetite was in the standard cubic crystal FM-3M with sides of 8.38 Å, confirming that Fe-loaded AB was impregnated with Fe_3O_4. The XRD pattern for Mg-loaded AB showed peaks corresponding to $Mg(OH)_2$, which showed the (001), (101), (102), (110), and (103) diffraction planes [37]. It was a hexagonal crystal with space group P-3m1 with a= 3.12 = b, c = 4.73 Å, and γ = 120.

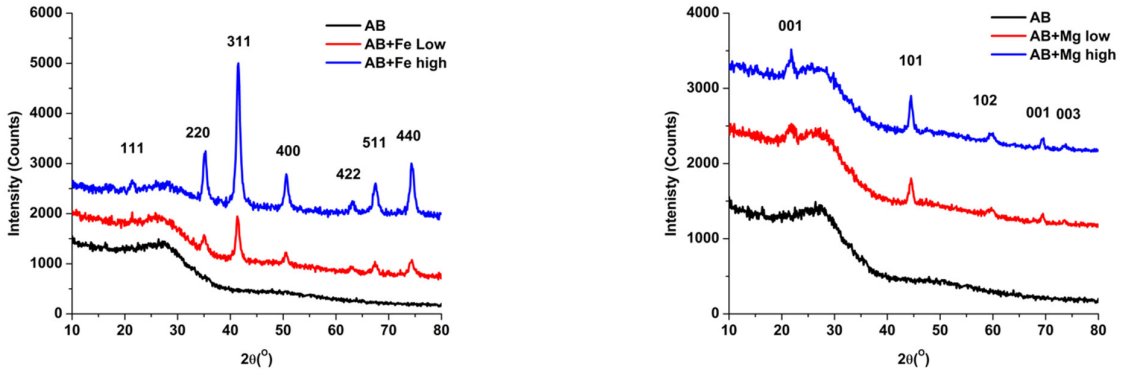

(**a**) (**b**)

Figure 1. XRD pattern of avocado seed biochar (AB): (**a**) Fe-loaded AB and (**b**) Mg-loaded AB.

As can be seen in Table 2, the Fe-loaded AB had a pH of 7.4–8.2, which was lower than that of modified biochar (8.8), while Mg-loaded AB showed a higher pH (9.7–9.9). The difference in pH reflects the original pH of the Fe chloride solution (pH < 2.0) and Mg chloride (pH~5.0) (Supplementary Figures S2 and S3). Proximate analysis results shed some insight on the mass distribution of biochar–metal composites (Table 2). Note that the ash content of a biochar represents inorganic mineral fractions, and the higher inclusion of metal oxide is expected to increase its ash content while decreasing fixed matter [38,39]. For example, unmodified AB showed an ash content at 6.8 %, and Mg-loaded AB showed a slightly higher level of ash content (8.1–8.5%). Fe-loaded AB, however, showed more than 5 times greater ash content (42% for AB + High Fe and 75% for AB + Low Fe), indicating the higher inclusion of Fe oxide (Fe_3O_4). Fixed matter (i.e., stable carbon portion from AB) was the opposite. Fe-loaded AB showed much lower fixed matter (<39%) than unmodified AB and Mg-loaded AB (62–72%). This result confirms that Fe-loaded AB contained a greater portion of metal oxide compared to its Mg counterpart. It is important to note that Mg-loaded AB showed distinct blue granules, indicating the presence of $Mg(OH)_2$, while the presence of Fe_3O_4 was not visually obvious in Fe-loaded AB other than a slight color change to very dark brown color (Figure 2).

Mg-loaded AB had a similar surface area (1.4–2.2 $m^2\ g^{-1}$) as unmodified AB (1.8 $m^2\ g^{-1}$). Fe-loaded AB had a more than 9-fold increase in the surface area, with AB + High Fe being the highest (49.9 $m^2\ g^{-1}$) followed by AB + Low Fe (17.1 $m^2\ g^{-1}$). Previous studies suggested that metal-loaded biochar decrease the surface area, possibly due to pore blockage with metal oxide precipitates, but this was not the case in the current study [13,40–42]. The surface area increased by Fe-loading the biochar, which has been reported in other studies [43,44]. Note that the same metal chloride loadings (high or low) were used for both Fe- and Mg-impregnation on AB in the current study (Table 1). In general, the increase in surface area in metal-loaded biochar is attributed to the smaller

sizes of the metal precipitates [17]. Thus, the enhanced surface area of Fe-loaded AB was likely due to the finer-size of Fe_3O_4 precipitates, particularly in AB + High Fe.

Table 2. Physicochemical properties of the avocado seed biochar (AB) materials.

	Unmodified AB	AB + High Fe	AB + Low Fe	AB + High Mg	AB + Low Mg
Volatile matter (%)	19.6	16.0	9.7	14.4	23.8
Ash (%)	6.8	42.1	75.0	8.1	8.5
Fixed matter (%)	71.6	38.5	12.6	71.7	62.3
Surface area ($m^2\ g^{-1}$)	1.8	49.9	17.1	1.4	2.2
pH	8.8	7.4	8.2	9.9	9.7

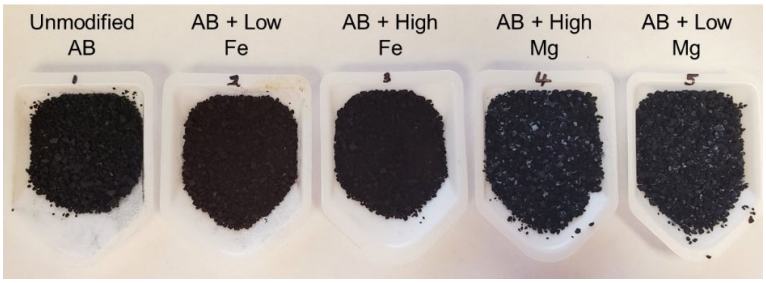

Figure 2. Avocado seed biochar (AB) samples after metal impregnation.

The SEM images showed that unmodified AB had honeycomb-like surface pore structures derived from avocado seed biomass (Figure 3). The pore size was approximately in the range of 20–100 µm in diameter. Fe-loaded AB showed an accumulation or coating of Fe_3O_4 precipitates onto the existing surfaces of AB, which was not evident in Mg-loaded AB.

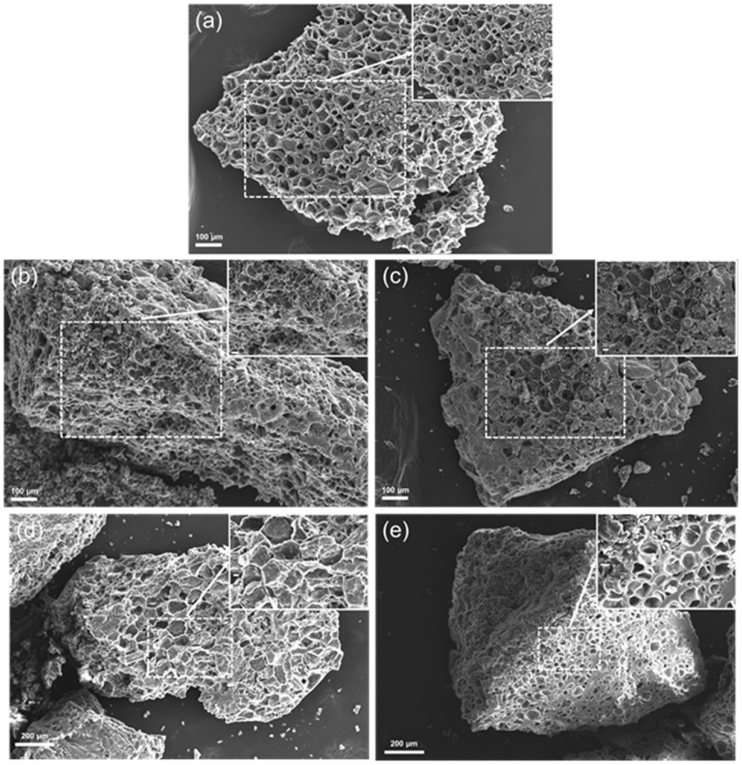

Figure 3. SEM images of avocado seed biochar (AB): (**a**) unmodified AB, (**b**) AB + High Fe, (**c**) AB + Low Fe, (**d**) AB + High Mg, and (**e**) AB + Low Mg.

Figure 4 shows the FTIR spectra of Fe- or Mg-loaded AB overlayed with unmodified AB. Overall, all biochar displayed broad peaks (3500–3200 cm^{-1}) by O–H stretching (water, H-bonded hydroxyl groups) to varying degrees, indicating the dehydration of cellulosic and ligneous components of AB [24,45]. The O–H stretching appeared to be more intense in Fe-loaded AB and less intense in Mg-loaded AB. It was notable that Mg-loaded AB showed a sharp peak at 3699 cm^{-1} (free O–H stretching; alcoholic and phenolic OH, not hydrogen bonded), reflecting the presence of $Mg(OH)_2$ [46]. Note that the current study did not measure FTIR after phosphate adsorption (spent biochar). A previous study found that the O–H group derived from the metal-loaded biochar became weaker, and a P–O peak appeared in the FTIR spectra after phosphate adsorption, indicating the group of O–H was replaced by P [19]. Aliphatic moieties (C–H stretching at 3050 cm^{-1}) were observed in unmodified AB and Fe-loaded AB (lesser extent), but the C–H stretching disappeared in Mg-loaded AB. All biochar displayed C=O stretching at 1740–1700 cm^{-1}, indicating carboxylic groups and traces of aldehydes, ketones, and esters [24,45]. Aromatic moieties (C=C stretching at 1600, 1510, and 1440 cm^{-1}; C–H bending at 885, 815, and 750 cm^{-1}) were observed in varying degrees in the fingerprint region [11,47].

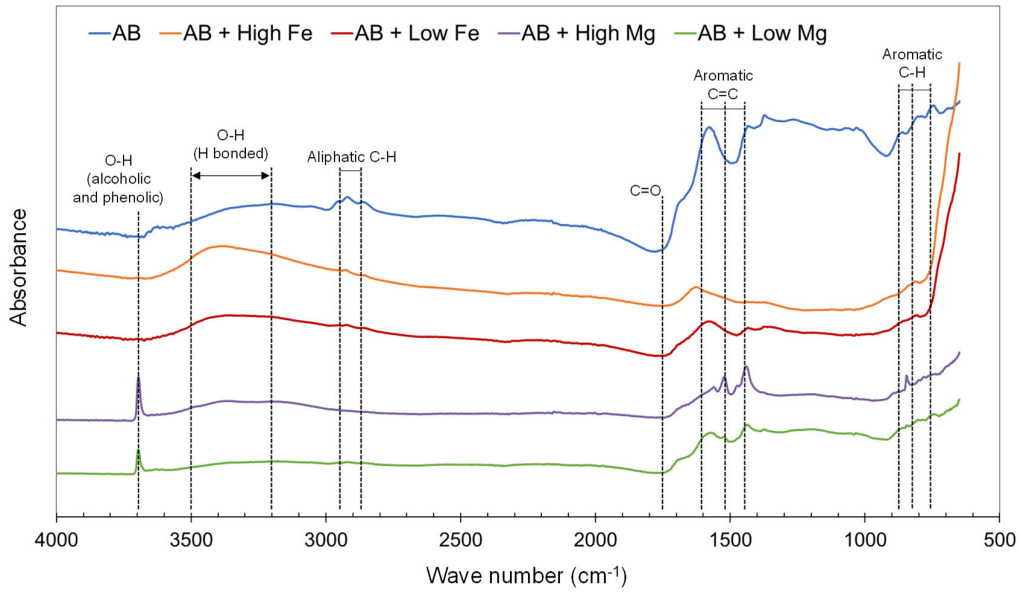

Figure 4. Fourier transform infrared (FTIR) spectra of avocado seed biochar (AB).

3.2. Intial pH Effect on Phosphate Adsorption

Unmodified AB equilibrated with 10 mg PO_4^{3-} L^{-1} showed no phosphate adsorption and released phosphate from the biochar itself, as noted in other studies of plant- or wood-based biochar (Figure 5) [7,48]. Thus, unmodified AB was not included for the phosphate adsorption isotherm. The greatest release of phosphate (25%) was found in the lowest pH (3.0). Overall, Fe-loaded AB (59–100%) showed higher phosphate adsorption than Mg-loaded AB (<41%) over a pH range of 3–11. For Fe-loaded AB, the phosphate adsorption decreased with an increasing pH, representing an adsorption envelope for anions [30]. According to the adsorption envelope phenomenon for anions, the Fe-loaded biochar surface becomes more protonated and positively charged with a decreasing pH, causing increased phosphate adsorption by electrostatic attraction. The phosphate adsorption is expected to decrease with an increasing pH due to the increased negatively charged surface, resulting in the electrostatic repulsion of phosphate [49]. Note that this study did not measure the point of zero charge (PZC). Assuming a PZC of magnetite at pH_{pzc}~6.5, it is expected that the surface charge of magnetite starts to become negatively charged at pH > 6.5, which is in agreement with the decreased phosphate adsorption at pH > 5.0 in the current study [50].

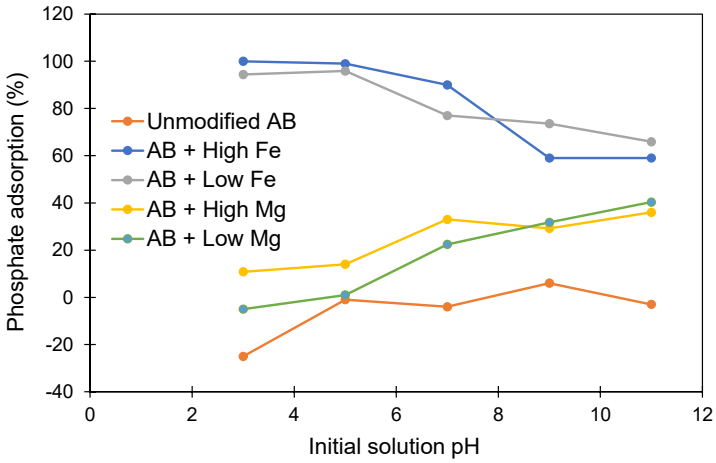

Figure 5. Phosphate adsorption affected by initial solution pH (3–11).

Mg-loaded AB showed the opposite trend, where phosphate adsorption increased with an increasing pH (Figure 5). Previous studies found that the pH_{pzc} of $Mg(OH)_2$-modified biochar was in the range of 10–12 [51–53]. According to this pH_{pzc}, the net charge of Mg-loaded AB in the current study is positively charged at pH < 10–12, and phosphate adsorption would increase progressively with a decreasing pH by electrostatic attraction [54]. However, this was not the case for the Mg-loaded AB in the current study. The precipitation of phosphate associated with $Mg(OH)_2$ was likely to occur with an increasing pH, resulting in increased phosphate adsorption (will be discussed more in the next section) [49].

3.3. Adsorption Isotherm

The phosphate adsorption data for Fe-loaded AB was explained better by the Langmuir model (R^2 = 0.91–0.96) than the Freundlich model (R^2 = 0.88–0.90) (Figure 6; Table 3). The S_{max} values (maximum phosphate adsorption capacity) of Fe-loaded AB were 15 mg g^{-1} for AB + High Fe and 12 mg g^{-1} for AB + Low Fe. It was notable that the Langmuir model did not explain well the phosphate adsorption by Mg-loaded AB (R^2 = 0.45–0.46), but the Freundlich model did (R^2 = 0.94–0.96). The goodness of model fittings was better with the Freundlich model in all cases when comparing AIC (Table 3). The S_{max} values of Mg-loaded AB were 30 mg g^{-1} for AB + High Mg and 40 mg g^{-1} for AB + Low Mg, but the validity of S_{max} values was questionable due to the poor fitting of measured data with the Langmuir model. Note that the Langmuir model assumes that adsorption occurs on a finite number of adsorption sites (monolayer coverage), allowing the estimation of S_{max} [27,30]. The Freundlich model is applicable for adsorption onto heterogenous surfaces with multiple stacking of adsorbates (multiple layer coverage), and the adsorption capacity is assumed to increase continuously with no adsorption maximum [55,56]. The distinct presence of $Mg(OH)_2$ granules in Mg-loaded AB (Figure 2) may explain the heterogenous nature of the surface and the better fitting with the Freundlich model. Note that the $1/n$ value from the Freundlich model indicates the surface heterogeneity of an adsorbent [27]. Mg-loaded AB (0.64–0.78) had more than two-times greater $1/n$ values than those of Fe-loaded AB (0.31–0.33), indicating the heterogeneous nature of surface adsorption sites in Mg-loaded AB.

The phosphate adsorption (Fe- vs. Mg-loaded AB) was higher with Fe-loaded AB in a low range of phosphate concentrations (≤50 mg L^{-1}) (Figure 6). For example, the amount of phosphate adsorbed after equilibrating 10 mg L^{-1} was in the order of AB + High Fe (2.7 mg g^{-1}) > AB + Low Fe (2.3 mg g^{-1}) > AB + High Mg (1.1 mg g^{-1}) > AB + Low Mg (1.0 mg g^{-1}). Overall, phosphate adsorption isotherm data by Mg-loaded AB followed an S-type isotherm, where at low concentrations, the surface has a low affinity for the adsorptive, which increases at higher concentrations [30]. For relative comparison,

the amount of phosphate adsorbed after equilibrating 500 mg L^{-1} was in the order of AB + Low Mg (32.0 mg g^{-1}) > AB + High Mg (30.0 mg g^{-1}) > AB + High Fe (14.2 mg g^{-1}) > AB + Low Fe (7.8 mg g^{-1}). These values were within the low end of reported phosphate sorption capacities for Fe-modified biochar (11–114 mg g^{-1}) and Mg-modified biochar (33–2720 mg g^{-1}) from the literature [6,54].

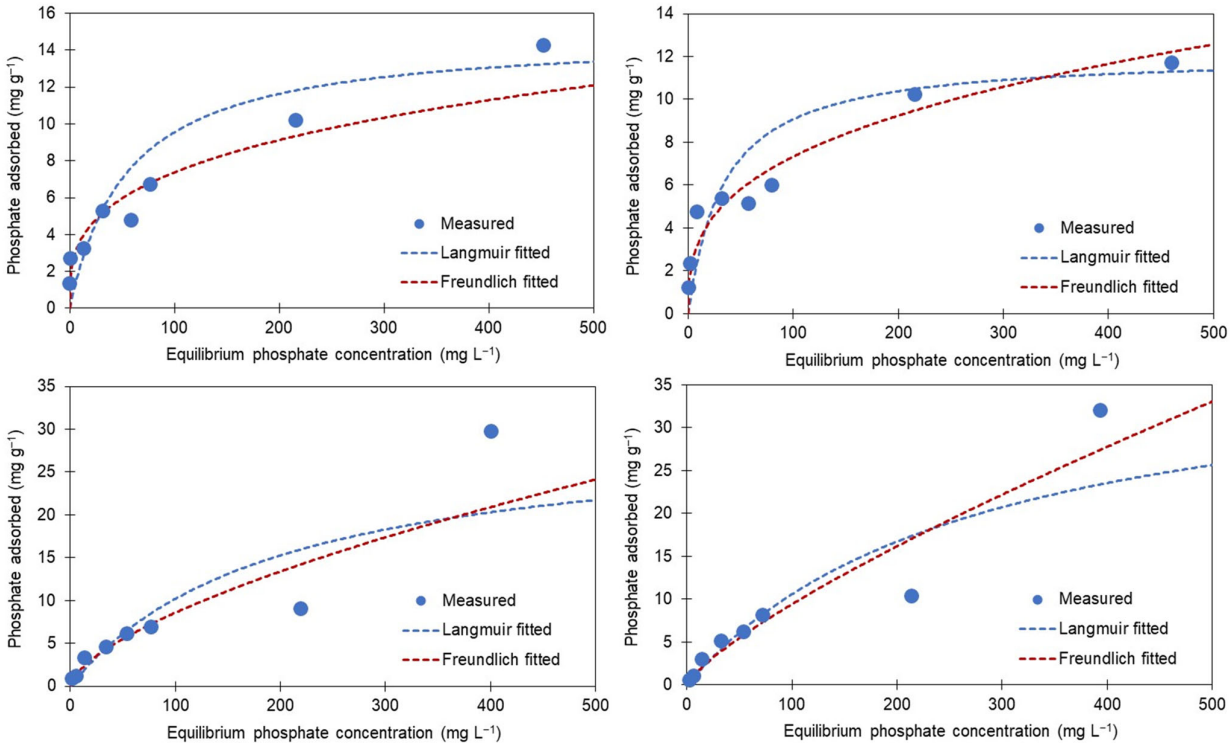

Figure 6. Phosphate adsorption isotherm fitted with the Langmuir and Freundlich models.

Table 3. Adsorption parameters estimated from the Langmuir and Freundlich adsorption models.

Model	Parameter	AB + High Fe	AB + Low Fe	AB + High Mg	AB + Low Mg
Langmuir	Linearized equation	y = 0.0763x + 3.7393 (R^2 = 0.91)	y = 0.0825x + 2.7632 (R^2 = 0.96)	y = 0.033x + 6.4971 (R^2 = 0.45)	y = 0.0251x + 6.9383 (R^2 = 0.46)
	S_{max} (mg g^{-1})	14.86	12.12	30.29	39.79
	K_L (L mg^{-1})	0.02	0.03	0.01	0.04
	CIA	32	24	145	127
Freundlich	Linearized equation	y = 0.2846x + 0.2691 (R^2 = 0.88)	y = 0.3408x + 0.1908 (R^2 = 0.90)	y = 0.6422x + 2.6492 (R^2 = 0.94)	y = 0.7797x + 2.4147 (R^2 = 0.96)
	K_F	1.80	1.57	446	260
	n	3.26	2.99	1.56	1.28
	$1/n$	0.31	0.33	0.64	0.78
	CIA	16	9	79	86

Main phosphate retention mechanisms by metal-loaded biochar include: (1) electrostatic attraction, (2) ligand exchange, (3) complexation, and (4) chemical precipitation [6,22,54]. While the current study does not reveal the exact mechanism, the enhanced phosphate adsorption by Mg-loaded AB in the high phosphate concentration range (75–500 mg L^{-1}) could be attributed to the precipitation of phosphate with dissolved Mg^{2+}. A previous study using $Mg(OH)_2/ZrO_2$ found that part of the impregnated $Mg(OH)_2$ was dissolved, and the presence of Mg^{2+} facilitated phosphate adsorption through the formation of an $Mg–PO_4–ZrO_2$ ternary inner-sphere complex [53]. Similar results were observed with a calcium (Ca^{2+})-rich biochar, where Ca^{2+} and HPO_4^- formed non-crystalline

$Ca_3(PO_4)_2$ precipitates, which converted to stable $Ca_5(OH)(PO_4)_3$(s) [49]. Note that the final solution's pH after phosphate adsorption isotherm was 6.8–7.8 for Fe-loaded AB, while it was 8.9–9.7 for Mg-loaded AB in the current study. Assuming metal-phosphate precipitation is favored at a high pH, a substantial portion of phosphate, particularly in the high phosphate concentration range, was likely to be removed by precipitation reactions in the Mg-loaded AB [40,57].

4. Conclusions

In this study, Fe- or Mg-loaded AB was generated by a post-pyrolysis, co-precipitation method and compared against unmodified AB for selected physicochemical properties and phosphate adsorption. Avocado seed was successful as a biochar feedstock material, and our results demonstrated clear benefits of the metal impregnation with regard to enhancing phosphate adsorption. This highlights its potential use for point-of-use water treatment (e.g., military use) where the source water is experiencing elevated levels of phosphate. Unmodified AB was not effective for phosphate adsorption and released phosphate more under acidic conditions. Fe-loaded AB performed better in low phosphate ranges ($\leq$50 mg L^{-1}); however, Mg-loaded AB outperformed Fe-loaded AB in high phosphate ranges (75–500 mg L^{-1}). The initial pH effect on phosphate adsorption followed a typical adsorption envelope of anions for Fe-loaded AB, indicating that electrostatic attraction played a key role for Fe-loaded AB. For Mg-loaded AB, the chemical precipitation of phosphate associated with dissolved Mg^{2+} was likely to play a key role for phosphate adsorption in high concentration ranges (75–500 mg L^{-1}). This study employed two loading levels (high and low) of metal impregnation, and the phosphate adsorption results did not show a significant benefit from high loading for metal impregnation. It is important to note that the current study did not perform kinetic experiments, phosphate desorption from the spent biochar, and the associated economics for phosphate removal and reuse. Further investigations addressing the biochar–metal dosage relationship for impregnation, different biochar feedstocks and pyrolysis conditions, testing under flowing conditions, and regeneration (desorption) aspects of phosphate are desirable to warrant Fe- or Mg-loaded biochar as a promising and sustainable sorbent for aqueous phosphate removal and their use as a slow-release fertilizer. The phosphate removal using similar metal-impregnated biochar should consider the local availability of biomass, pyrolysis conditions, metal impregnation processes, and potential economics of the spent biochar.

Supplementary Materials: The following supporting information can be downloaded at: https://www.mdpi.com/article/10.3390/cleantechnol4030042/s1, Figure S1: Avocado seed biochar (AB) preparation; Figure S2: Preparation of Fe-loaded avocado seed biochar; Figure S3: Preparation of Mg-loaded avocado seed biochar.

Author Contributions: Conceptualization, J.J.K., S.G. and D.T.T.; experimental design, J.J.K., S.G. and D.T.T.; performance of experiments, J.J.K. and J.P.; Data analysis, J.J.K., J.P., S.G. and D.T.T.; writing—original draft preparation, J.J.K., writing—review and editing, J.J.K., J.P., S.G. and D.T.T. All authors have read and agreed to the published version of the manuscript.

Funding: This study was supported by Historically Black Colleges and Universities (HBCU)/Minority Institutions (MI) Summer Faculty Research Fellowship Program sponsored by the U.S. Department of Defense (DoD), and the grant number is 169642.

Institutional Review Board Statement: Not applicable.

Informed Consent Statement: Not applicable.

Data Availability Statement: Derived data supporting the findings of this study are available from the corresponding author (J.J.K.) upon request.

Conflicts of Interest: The authors declare no conflict of interest.

References

1. Sharpley, A. Managing Agricultural Phosphorus to Minimize Water Quality Impacts. *Sci. Agric.* **2016**, *73*, 1–8. [CrossRef]
2. Correll, D. Phosphorus: A Rate Limiting Nutrient in Surface Waters. *Poult. Sci.* **1999**, *78*, 674–682. [CrossRef] [PubMed]
3. Carpenter, S.R. Eutrophication of Aquatic Ecosystems: Bistability and Soil Phosphorus. *Proc. Natl. Acad. Sci. USA* **2005**, *102*, 10002–10005. [CrossRef] [PubMed]
4. Litke, D.W. *Review of Phosphorus Control Measures in the United States and Their Effects on Water Quality*; US Department of the Interior, US Geological Survey: Denver, CO, USA, 1999.
5. Bunce, J.T.; Ndam, E.; Ofiteru, I.D.; Moore, A.; Graham, D.W. A Review of Phosphorus Removal Technologies and Their Applicability to Small-Scale Domestic Wastewater Treatment Systems. *Front. Environ. Sci.* **2018**, *6*, 8. [CrossRef]
6. Vikrant, K.; Kim, K.-H.; Ok, Y.S.; Tsang, D.C.W.; Tsang, Y.F.; Giri, B.S.; Singh, R.S. Engineered/Designer Biochar for the Removal of Phosphate in Water and Wastewater. *Sci. Total Environ.* **2018**, *616–617*, 1242–1260. [CrossRef] [PubMed]
7. Almanassra, I.W.; Mckay, G.; Kochkodan, V.; Atieh, M.A.; Al-Ansari, T. A State of the Art Review on Phosphate Removal from Water by Biochars. *Chem. Eng. J.* **2021**, *409*, 128211. [CrossRef]
8. Almanassra, I.W.; Kochkodan, V.; Subeh, M.; Mckay, G.; Atieh, M.; Al-Ansari, T. Phosphate Removal from Synthetic and Treated Sewage Effluent by Carbide Derive Carbon. *J. Water Process Eng.* **2020**, *36*, 101323. [CrossRef]
9. Hauda, J.K.; Safferman, S.I.; Ghane, E. Adsorption Media for the Removal of Soluble Phosphorus from Subsurface Drainage Water. *Int. J. Environ. Res. Public Health* **2020**, *17*, 7693. [CrossRef]
10. Finn, M.; Rodriguez, R.; Contrino, D.; Swenson, J.; Mazyck, D.W.; Suau, S. Impact of Inherent Magnesium in Biochar for Phosphate Removal from Reclaimed Water Streams. *J. Environ. Eng.* **2022**, *148*, 04021085. [CrossRef]
11. Mireles, S.; Parsons, J.; Trad, T.; Cheng, C.-L.; Kang, J. Lead Removal from Aqueous Solutions Using Biochars Derived from Corn Stover, Orange Peel, and Pistachio Shell. *Int. J. Environ. Sci. Technol.* **2019**, *16*, 5817–5826. [CrossRef]
12. Dai, S.; Zhao, Y.; Niu, D.; Li, Q.; Chen, Y. Preparation and Reactivation of Magnetic Biochar by Molten Salt Method: Relevant Performance for Chlorine-Containing Pesticides Abatement. *J. Air Waste Manag. Assoc.* **2019**, *69*, 58–70. [CrossRef] [PubMed]
13. Sizmur, T.; Fresno, T.; Akgül, G.; Frost, H.; Moreno-Jiménez, E. Biochar Modification to Enhance Sorption of Inorganics from Water. *Bioresour. Technol.* **2017**, *246*, 34–47. [CrossRef]
14. Thines, K.R.; Abdullah, E.C.; Mubarak, N.M.; Ruthiraan, M. Synthesis of Magnetic Biochar from Agricultural Waste Biomass to Enhancing Route for Waste Water and Polymer Application: A Review. *Renew. Sustain. Energy Rev.* **2017**, *67*, 257–276. [CrossRef]
15. Zhao, R.-S.; Liu, Y.-L.; Chen, X.-F.; Yuan, J.-P.; Bai, A.-Y.; Zhou, J.-B. Preconcentration and Determination of Polybrominated Diphenyl Ethers in Environmental Water Samples by Solid-Phase Microextraction with Fe3O4-Coated Bamboo Charcoal Fibers Prior to Gas Chromatography–Mass Spectrometry. *Anal. Chim. Acta* **2013**, *769*, 65–71. [CrossRef] [PubMed]
16. Jun, B.-M.; Kim, Y.; Han, J.; Yoon, Y.; Kim, J.; Park, C.M. Preparation of Activated Biochar-Supported Magnetite Composite for Adsorption of Polychlorinated Phenols from Aqueous Solutions. *Water* **2019**, *11*, 1899. [CrossRef]
17. Hou, L.; Liang, Q.; Wang, F. Mechanisms That Control the Adsorption–Desorption Behavior of Phosphate on Magnetite Nanoparticles: The Role of Particle Size and Surface Chemistry Characteristics. *RSC Adv.* **2020**, *10*, 2378–2388. [CrossRef]
18. Li, A.; Ge, W.; Liu, L.; Qiu, G. Preparation, Adsorption Performance and Mechanism of MgO-Loaded Biochar in Wastewater Treatment: A Review. *Environ. Res.* **2022**, *212*, 113341. [CrossRef] [PubMed]
19. Yang, Q.; Wang, X.; Luo, W.; Sun, J.; Xu, Q.; Chen, F.; Zhao, J.; Wang, S.; Yao, F.; Wang, D.; et al. Effectiveness and Mechanisms of Phosphate Adsorption on Iron-Modified Biochars Derived from Waste Activated Sludge. *Bioresour. Technol.* **2018**, *247*, 537–544. [CrossRef] [PubMed]
20. Yao, Y.; Gao, B.; Inyang, M.; Zimmerman, A.R.; Cao, X.; Pullammanappallil, P.; Yang, L. Removal of Phosphate from Aqueous Solution by Biochar Derived from Anaerobically Digested Sugar Beet Tailings. *J. Hazard. Mater.* **2011**, *190*, 501–507. [CrossRef]
21. Fang, C.; Zhang, T.; Li, P.; Jiang, R.; Wang, Y. Application of Magnesium Modified Corn Biochar for Phosphorus Removal and Recovery from Swine Wastewater. *Int. J. Environ. Res. Public Health* **2014**, *11*, 9217–9237. [CrossRef] [PubMed]
22. Yao, Y.; Gao, B.; Chen, J.; Yang, L. Engineered Biochar Reclaiming Phosphate from Aqueous Solutions: Mechanisms and Potential Application as a Slow-Release Fertilizer. *Environ. Sci. Technol.* **2013**, *47*, 8700–8708. [CrossRef] [PubMed]
23. García-Vargas, M.C.; del Mar Contreras, M.; Castro, E. Avocado-Derived Biomass as a Source of Bioenergy and Bioproducts. *Appl. Sci.* **2020**, *10*, 8195. [CrossRef]
24. Granados, P.; Mireles, S.; Pereira, E.; Cheng, C.-L.; Kang, J.J. Effects of Biochar Production Methods and Biomass Types on Lead Removal from Aqueous Solution. *Appl. Sci.* **2022**, *12*, 5040. [CrossRef]
25. Matos, T.; Schultz, J.; Khan, M.; Zanoelo, E.; Mangrich, A.; Araújo, B.; Navickiene, S.; Romão, L. Using Magnetized (Fe_3O_4/Biochar Nanocomposites) and Activated Biochar as Adsorbents to Remove Two Neuro-Active Pesticides from Waters. *J. Braz. Chem. Soc.* **2017**, *28*, 1975–1987. [CrossRef]
26. Chen, B.; Chen, Z.; Lv, S. A Novel Magnetic Biochar Efficiently Sorbs Organic Pollutants and Phosphate. *Bioresour. Technol.* **2011**, *102*, 716–723. [CrossRef] [PubMed]
27. Tomin, O.; Yazdani, M.R. Production and Characterization of Porous Magnetic Biochar: Before and after Phosphate Adsorption Insights. *J. Porous Mater.* **2022**, *29*, 849–859. [CrossRef]
28. Karunanithi, R.; Ok, Y.S.; Dharmarajan, R.; Ahmad, M.; Seshadri, B.; Bolan, N.; Naidu, R. Sorption, Kinetics and Thermodynamics of Phosphate Sorption onto Soybean Stover Derived Biochar. *Environ. Technol. Innov.* **2017**, *8*, 113–125. [CrossRef]

29. Essington, M.E. *Soil and Water Chemistry: An Integrative Approach*, 2nd ed.; First Issued in Paperback; CRC Press: Boca Raton, FL, USA; Taylor & Francis Group: Abingdon, UK, 2021; ISBN 978-1-03-209869-2.
30. Sparks, D.L. *Environmental Soil Chemistry*, 2nd ed.; Academic Press: Amsterdam, The Netherlands; Boston, FL, USA, 2003; ISBN 978-0-12-656446-4.
31. Kim, W.-K.; Shim, T.; Kim, Y.-S.; Hyun, S.; Ryu, C.; Park, Y.-K.; Jung, J. Characterization of Cadmium Removal from Aqueous Solution by Biochar Produced from a Giant Miscanthus at Different Pyrolytic Temperatures. *Bioresour. Technol.* **2013**, *138*, 266–270. [CrossRef] [PubMed]
32. Eljamal, O.; Eljamal, R.; Maamoun, I.; Khalil, A.M.E.; Shubair, T.; Falyouna, O.; Sugihara, Y. Efficient Treatment of Ammonia-Nitrogen Contaminated Waters by Nano Zero-Valent Iron/Zeolite Composite. *Chemosphere* **2022**, *287*, 131990. [CrossRef] [PubMed]
33. Maamoun, I.; Bensaida, K.; Eljamal, R.; Falyouna, O.; Tanaka, K.; Tosco, T.; Sugihara, Y.; Eljamal, O. Rapid and Efficient Chromium (VI) Removal from Aqueous Solutions Using Nickel Hydroxide Nanoplates (NNiHs). *J. Mol. Liq.* **2022**, *358*, 119216. [CrossRef]
34. Akaike, H. A New Look at the Statistical Model Identification. *IEEE Trans. Automat. Contr.* **1974**, *19*, 716–723. [CrossRef]
35. Loh, K.-S.; Lee, Y.; Musa, A.; Salmah, A.; Zamri, I. Use of Fe_3O_4 Nanoparticles for Enhancement of Biosensor Response to the Herbicide 2,4-Dichlorophenoxyacetic Acid. *Sensors* **2008**, *8*, 5775–5791. [CrossRef] [PubMed]
36. Faiyas, A.P.A.; Vinod, E.M.; Joseph, J.; Ganesan, R.; Pandey, R.K. Dependence of PH and Surfactant Effect in the Synthesis of Magnetite (Fe_3O_4) Nanoparticles and Its Properties. *J. Magn. Magn. Mater.* **2010**, *322*, 400–404. [CrossRef]
37. Deng, Y.; Li, X.; Ni, F.; Liu, Q.; Yang, Y.; Wang, M.; Ao, T.; Chen, W. Synthesis of Magnesium Modified Biochar for Removing Copper, Lead and Cadmium in Single and Binary Systems from Aqueous Solutions: Adsorption Mechanism. *Water* **2021**, *13*, 599. [CrossRef]
38. Buss, W.; Jansson, S.; Mašek, O. Unexplored Potential of Novel Biochar-Ash Composites for Use as Organo-Mineral Fertilizers. *J. Clean. Prod.* **2019**, *208*, 960–967. [CrossRef]
39. Xu, X.; Zhao, Y.; Sima, J.; Zhao, L.; Mašek, O.; Cao, X. Indispensable Role of Biochar-Inherent Mineral Constituents in Its Environmental Applications: A Review. *Bioresour. Technol.* **2017**, *241*, 887–899. [CrossRef] [PubMed]
40. Ajmal, Z.; Muhmood, A.; Dong, R.; Wu, S. Probing the Efficiency of Magnetically Modified Biomass-Derived Biochar for Effective Phosphate Removal. *J. Environ. Manag.* **2020**, *253*, 109730. [CrossRef] [PubMed]
41. Cui, Q.; Jiao, G.; Zheng, J.; Wang, T.; Wu, G.; Li, G. Synthesis of a Novel Magnetic *Caragana Korshinskii* Biochar/Mg–Al Layered Double Hydroxide Composite and Its Strong Adsorption of Phosphate in Aqueous Solutions. *RSC Adv.* **2019**, *9*, 18641–18651. [CrossRef] [PubMed]
42. Karunanayake, A.G.; Navarathna, C.M.; Gunatilake, S.R.; Crowley, M.; Anderson, R.; Mohan, D.; Perez, F.; Pittman, C.U.; Mlsna, T. Fe_3O_4 Nanoparticles Dispersed on Douglas Fir Biochar for Phosphate Sorption. *ACS Appl. Nano Mater.* **2019**, *2*, 3467–3479. [CrossRef]
43. Mohan, D.; Kumar, H.; Sarswat, A.; Alexandre-Franco, M.; Pittman, C.U. Cadmium and Lead Remediation Using Magnetic Oak Wood and Oak Bark Fast Pyrolysis Bio-Chars. *Chem. Eng. J.* **2014**, *236*, 513–528. [CrossRef]
44. Baig, S.A.; Zhu, J.; Muhammad, N.; Sheng, T.; Xu, X. Effect of Synthesis Methods on Magnetic Kans Grass Biochar for Enhanced As(III, V) Adsorption from Aqueous Solutions. *Biomass Bioenergy* **2014**, *71*, 299–310. [CrossRef]
45. Keiluweit, M.; Nico, P.S.; Johnson, M.G.; Kleber, M. Dynamic Molecular Structure of Plant Biomass-Derived Black Carbon (Biochar). *Environ. Sci. Technol.* **2010**, *44*, 1247–1253. [CrossRef]
46. Zahir, M.H.; Rahman, M.M.; Irshad, K.; Rahman, M.M. Shape-Stabilized Phase Change Materials for Solar Energy Storage: MgO and $Mg(OH)_2$ Mixed with Polyethylene Glycol. *Nanomaterials* **2019**, *9*, 1773. [CrossRef] [PubMed]
47. Uchimiya, M.; Wartelle, L.H.; Klasson, K.T.; Fortier, C.A.; Lima, I.M. Influence of Pyrolysis Temperature on Biochar Property and Function as a Heavy Metal Sorbent in Soil. *J. Agric. Food Chem.* **2011**, *59*, 2501–2510. [CrossRef]
48. Yao, Y.; Gao, B.; Zhang, M.; Inyang, M.; Zimmerman, A.R. Effect of Biochar Amendment on Sorption and Leaching of Nitrate, Ammonium, and Phosphate in a Sandy Soil. *Chemosphere* **2012**, *89*, 1467–1471. [CrossRef] [PubMed]
49. Qiu, G.; Zhao, Y.; Wang, H.; Tan, X.; Chen, F.; Hu, X. Biochar Synthesized via Pyrolysis of Broussonetia Papyrifera Leaves: Mechanisms and Potential Applications for Phosphate Removal. *Env. Sci. Pollut. Res.* **2019**, *26*, 6565–6575. [CrossRef] [PubMed]
50. Milonjić, S.K.; Kopečni, M.M.; Ilić, Z.E. The Point of Zero Charge and Adsorption Properties of Natural Magnetite. *J. Radioanal. Chem.* **1983**, *78*, 15–24. [CrossRef]
51. Lin, J.X.; Wang, L. Adsorption of Dyes Using Magnesium Hydroxide-Modified Diatomite. *Desalination Water Treat.* **2009**, *8*, 263–271. [CrossRef]
52. Tao, X.; Huang, T.; Lv, B. Synthesis of Fe/Mg-Biochar Nanocomposites for Phosphate Removal. *Materials* **2020**, *13*, 816. [CrossRef]
53. Lin, J.; He, S.; Wang, X.; Zhang, H.; Zhan, Y. Removal of Phosphate from Aqueous Solution by a Novel $Mg(OH)_2/ZrO_2$ Composite: Adsorption Behavior and Mechanism. *Colloids Surf. A Physicochem. Eng. Asp.* **2019**, *561*, 301–314. [CrossRef]
54. Wang, J.; Zhang, G.; Qiao, S.; Zhou, J. Magnetic Fe0/Iron Oxide-Coated Diatomite as a Highly Efficient Adsorbent for Recovering Phosphorus from Water. *Chem. Eng. J.* **2021**, *412*, 128696. [CrossRef]
55. Wu, Q.; Xian, Y.; He, Z.; Zhang, Q.; Wu, J.; Yang, G.; Zhang, X.; Qi, H.; Ma, J.; Xiao, Y.; et al. Adsorption Characteristics of Pb(II) Using Biochar Derived from Spent Mushroom Substrate. *Sci. Rep.* **2019**, *9*, 15999. [CrossRef] [PubMed]

56. Alves, B.S.Q.; Fernandes, L.A.; Southard, R.J. Biochar-Cadmium Retention and Its Effects after Aging with Hydrogen Peroxide (H_2O_2). *Heliyon* **2021**, *7*, e08476. [CrossRef] [PubMed]
57. Daneshgar, S.; Buttafava, A.; Capsoni, D.; Callegari, A.; Capodaglio, A. Impact of PH and Ionic Molar Ratios on Phosphorous Forms Precipitation and Recovery from Different Wastewater Sludges. *Resources* **2018**, *7*, 71. [CrossRef]